What Controls the Entrainment Rate of Dry Buoyant Thermals with Varying Initial Aspect Ratio?

HUGH MORRISON,[a] NADIR JEEVANJEE,[b] DANIEL LECOANET,[c] AND JOHN M. PETERS[d]

[a] National Center for Atmospheric Research, Boulder, Colorado
[b] Geophysical Fluid Dynamics Laboratory, Princeton, New Jersey
[c] Department of Engineering Sciences and Applied Mathematics, Northwestern University, Evanston, Illinois
[d] Department of Meteorology and Atmospheric Science, The Pennsylvania State University, University Park, Pennsylvania

(Manuscript received 5 April 2023, in final form 26 August 2023, accepted 30 August 2023)

ABSTRACT: This study uses theory and numerical simulations to analyze the nondimensional spreading rate α (change in radius with height) of buoyant thermals as they rise and entrain surrounding environmental fluid. A focus is on how α varies with initial thermal aspect ratio A_r, defined as height divided by width of the initial buoyancy perturbation. An analytic equation for thermal ascent rate w_t that depends on α is derived from the thermal-volume-averaged momentum budget equation. The thermal top height when w_t is maximum, defining a critical height z_c, is inversely proportional to α. The height z_c also corresponds to the thermal top height when buoyant fluid along the thermal's vertical axis is fully replaced by entrained nonbuoyant environmental fluid rising from below the thermal. The time scale for this process is controlled by the vertical velocity of parcels rising upward through the thermal's core. This parcel vertical velocity is approximated from Hill's analytic spherical vortex, yielding an analytic inverse relation between α and A_r. Physically, this α–A_r relation is connected to changes in circulation as A_r is modified. Numerical simulations of thermals with A_r varied from 0.5 to 2 give α values close to the analytic theoretical relation, with a factor of ~3 decrease in α as A_r is increased from 0.5 to 2. The theory also explains why α of initially spherical thermals from past laboratory and modeling studies is about 0.15. Overall, this study provides a theoretical underpinning for understanding the entrainment behavior of thermals, relevant to buoyantly driven atmospheric flows.

SIGNIFICANCE STATEMENT: Thermals, which are coherent, quasi-spherical regions of upward-moving buoyant fluid, are a key feature of many convective atmospheric flows. The purpose of this study is to characterize how thermals entrain surrounding fluid and spread out as they rise. We use theory and numerical modeling to explain why entrainment rate decreases with an increase in the initial thermal aspect ratio—the ratio of height to width. This work also explains why the nondimensional spreading rate (change in thermal radius with height) of initially spherical thermals from past laboratory and numerical modeling studies is about 0.15. Overall, this work provides a framework for conceptualizing the entrainment behavior of thermals and thus improved understanding of vertical transport in convective atmospheric flows.

KEYWORDS: Buoyancy; Entrainment; Small scale processes; Vertical motion; Vortices

1. Introduction

Thermals—coherent, isolated, quasi-spherical regions of upward-moving buoyant fluid—are a common feature of convective atmospheric flows. A key characteristic of thermals is the rate at which they increase in size as they ascend owing to entrainment of the surrounding fluid. Assuming thermal shape is self-similar (meaning that thermals do not change shape over time), dimensional analysis shows that thermal radius R is proportional to thermal top height z_t, that is, dR/dz_t is constant[1] (e.g., Scorer 1957). (Note that all symbols used in the paper are defined in the appendix.) Numerous laboratory and numerical modeling studies have supported this basic scaling (e.g., Scorer 1957; Richards 1961; Bond and Johari 2005; Zhao et al. 2013; Lai et al. 2015; Lecoanet and Jeevanjee 2019, hereinafter LJ2019; McKim et al. 2020; Morrison et al. 2021).

The rate of increase in R is closely related to the entrainment rate of thermals. From LJ2019, a thermal net fractional entrainment rate is defined as $\epsilon \equiv d(\ln V)/dz_t$, where V is the thermal volume. Combined with self-similarity, this gives $\epsilon = 3\alpha/R$, where $\alpha \equiv dR/dz_t$. We emphasize that ϵ in this case is a *net* fractional entrainment rate because thermal volume is impacted by both entrainment (inflow of environmental fluid) and detrainment (outflow of thermal fluid). However, LJ2019 showed that detrainment is negligible for both laminar and turbulent dry, initially spherical thermals in a neutrally stable environment. Thus, ϵ provides a close approximation for total entrainment in such conditions. An entrainment efficiency can also be defined as $e \equiv \epsilon R$, which gives $e = 3\alpha$ for self-similar thermals.

[1] Note that constant dR/dz_t following self-similarity and dimensional analysis is valid when there are no other physical length scales. It follows that this scaling applies to dry thermals in an unstratified environment within an infinite domain.

Corresponding author: Hugh Morrison, morrison@ucar.edu

DOI: 10.1175/JAS-D-23-0063.1

Thermals entrain by a process of drawing in fluid mainly from below the thermal (e.g., LJ2019; Zhao et al. 2013; McKim et al. 2020; Morrison et al. 2021). As a thermal spins up, buoyancy becomes concentrated near the center of rotation in the thermal's toroidal circulation (i.e., vortex ring core); see Fig. 1 for a schematic of thermal structure. As a result, there is baroclinic generation of buoyancy on the outside edge of the vortex ring and destruction on the inside edge that lead to a spreading of the vortex (McKim et al. 2020). Moreover, without buoyant fluid present along the thermal's vertical axis, circulation is nearly constant. This implies a basic constraint on the spreading rate of thermals following the principle of momentum conservation (Turner 1957). Specifically, buoyant vortex rings (which form the core of thermals) must expand over time to conserve momentum, with the rate of spread determined by the thermal-integrated buoyant forcing and the circulation. McKim et al. (2020) combined the buoyant vortex ring argument of Turner (1957) with the thermal's vertical momentum equation to derive an analytic model for the vertical velocity of thermal top w_t, R, and buoyancy B at any time past spinup that does not rely on empirically determined parameters, provided w_t, R, and B are known at the time when the thermal is spun up.

While the basic mechanism of thermal entrainment and spreading is well understood, factors controlling the spreading rate are not. Lai et al. (2015) combined a relation between circulation, impulse (related to time-integrated buoyant forcing), and thermal spreading rate with an empirical power-law relation between normalized circulation and initial thermal aspect ratio A_r to predict α from A_r. They showed that variations in A_r for spheroidal thermals from ~0.5 to 2 lead to substantial variability in α, from about 0.1 to 0.3. These results are consistent with laboratory experiments reporting a similar range of α (e.g., Scorer 1957; Escudier and Maxworthy 1973; Bond and Johari 2005, 2010; Zhao et al. 2013). A consensus from laboratory and numerical modeling studies is that $\alpha \approx 0.12$–0.18 for initially spherical thermals in an unstratified environment (e.g., LJ2019; Bond and Johari 2010; Zhao et al. 2013; Lai et al. 2015). Values are ~0.2–0.3 for initially oblate thermals with $A_r < 1$ and smaller for prolate thermals with $A_r > 1$, ~0.1–0.15 (see Fig. 17 of Lai et al. 2015). There is little sensitivity of α to initial aspect ratio for $A_r > 2$ (Bond and Johari 2005). Modifying other aspects of thermal initial conditions can also produce variability in α, such as having an initial circulation (Escudier and Maxworthy 1973). Note that α may also depend on the Reynolds number R_e of the flow, although LJ2019 showed with direct numerical simulation (DNS) that the basic mechanism of entrainment is the same for laminar and turbulent thermals (R_e of 630 and 6300, respectively), and α was only ~20% higher for turbulent thermals. Their results indicate that turbulence is not necessary for entrainment and that the primary mechanism for entrainment is organized inflow controlled by the thermal's buoyancy distribution.

The above discussion raises two important science questions. First, why do initially spherical thermals in an unstratified environment (and initially motionless) have $\alpha \approx 0.15$? Why this particular value, and what are the physical mechanisms explaining it? Second, why does the spreading rate of thermals as they rise (α) increase as their initial aspect (A_r) is decreased? To our knowledge, all previous studies have relied in some way on empirical constraint to obtain parameters, from either laboratory experiments or numerical modeling, at least during the spinup phase which is crucial for predicting α. In this study, we derive an expression for α as a function of A_r that does not rely on such empirically determined parameters. The goal is to predict α from A_r from the basic equations to provide a theoretical underpinning for understanding factors controlling the thermal spreading rate. The predicted values of α are compared to those obtained from numerical simulations of thermals over a range of A_r.

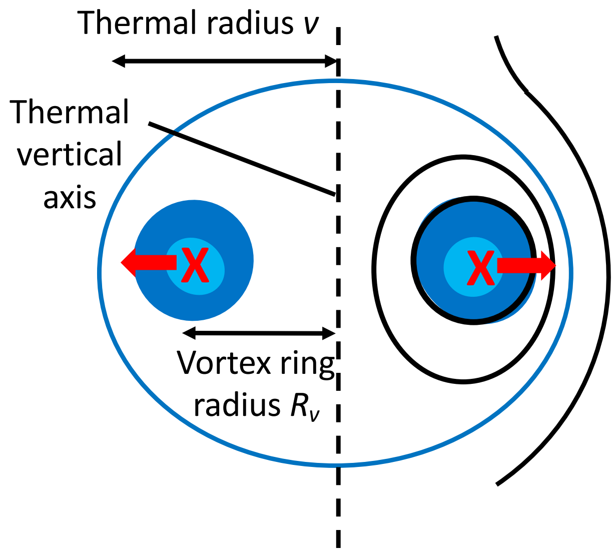

FIG. 1. Schematic diagram of a vertical cross section through the thermal center. The central vertical axis is indicated by the dashed line. Red X symbols mark the center of circulation comprising the vortex ring core with radius R_v. After spinup, the region of nonzero buoyancy indicated by blue shading is confined to the vortex ring core. Baroclinic generation and destruction of vorticity associated with this buoyancy structure leads to outward spreading of the vortex ring structure and thermal as a whole as shown by the red arrows. Black curved lines illustrate streamfunction isolines (only shown for the right half of the thermal). The thermal boundary, which is also a streamfunction isoline, is indicated by the curved blue line. This boundary also defines the thermal radius R.

In the theoretical part, we first derive an analytic expression for thermal ascent rate w_t from the nondimensional thermal momentum budget equation. We then use this expression to derive an analytic relation between α and the thermal spinup height z_c (defined as the thermal top height when w_t reaches a maximum), valid over a range of initial thermal aspect ratios. We show that z_c also corresponds to the time for parcels initially near the thermal bottom to ascend through the thermal core to near the thermal top. This determines the time for buoyancy to be removed from the central thermal core by entrainment of nonbuoyant environmental fluid, after which circulation is nearly constant. This time scale for thermal spinup depends linearly on A_r and is determined by the thermal's internal flow structure which is well modeled by Hill's analytic spherical vortex (Hill 1894) even for nonspherical thermals. We show that the predicted values of w_t, α, and z_c are consistent with numerical simulations of buoyant thermals over a range of A_r from 0.5 to 2.

The paper is organized as follows. Section 2 provides a theoretical description of the problem and derivation of equations for w_t and α. Section 3 gives a description of the numerical model and experimental design. Section 4 presents results from the numerical simulations and comparison of these results with theory. A summary and conclusions are given in section 5.

2. Theoretical description

We first write the basic governing equations that set the stage for the rest of the derivation. These are the incompressible Boussinesq–Euler equations for fluid motion and mass continuity plus the conservation equation for perturbation fluid density:

$$\frac{\partial \mathbf{u}}{\partial t} + \mathbf{u}\cdot\nabla\mathbf{u} = -\rho_0^{-1}\nabla p - \frac{\rho'}{\rho_0}g\hat{\mathbf{k}}, \tag{1}$$

$$\nabla\cdot\mathbf{u} = 0, \tag{2}$$

$$\frac{\partial \rho'}{\partial t} + \mathbf{u}\cdot\nabla\rho' = 0, \tag{3}$$

where t is the time, $\mathbf{u}$ is the velocity vector, $\hat{\mathbf{k}}$ is a unit vector pointed in the vertical (opposite to the direction of gravitational acceleration), p is the pressure, ρ_0 is a constant background fluid density, ρ' is a perturbation fluid density from the background density, and g is the gravitational acceleration. Here, the environment is assumed to be neutrally stable; for inviscid flow in a neutrally stable environment and applying the incompressible Boussinesq approximation, the perturbation density acts as a fluid tracer with no sources or sinks. In the following, we use buoyancy defined as $B \equiv -g\rho'/\rho_0$.

a. Thermal momentum budget

To derive our analytic thermal model and theoretical values for α, we first focus on the vertical momentum budget of thermals. This allows us to derive an analytic expression for the thermal ascent rate, from which we obtain expressions for thermal spreading rate α later. Defining the thermal as occupying some portion of space defined by Ω within the domain, we can integrate over Ω to obtain the thermal's budget of vertical momentum $\rho_0 w$, where w is the vertical velocity. Because Ω changes over time, we use Gauss's theorem to relate the divergence of the momentum field over Ω to the flux of momentum across the surface of Ω (Romps and Charn 2015; Morrison et al. 2022):

$$\frac{d}{dt}\int_{\Omega(t)}\rho_0 w d^3x = -\int_{\Omega(t)}\frac{\partial p}{\partial z}d^3x + \int_{\Omega(t)}\rho_0 B d^3x + \int_{\partial\Omega(t)}(\hat{\mathbf{n}}\cdot\mathbf{u}_e)\rho_0 w d^2x, \tag{4}$$

where $\partial\Omega(t)$ is the two-dimensional boundary of $\Omega(t)$, $\hat{\mathbf{n}}$ is a unit vector normal to the thermal's surface, and $\mathbf{u}_e$ is an effective entrainment velocity defined as the displacement rate of the thermal boundary $\mathbf{u}_b$ relative to flow velocity $\mathbf{u}$, i.e., $\mathbf{u}_e = \mathbf{u}_b - \mathbf{u}$.

Defining $\overline{w} \equiv V^{-1}\int_{\Omega(t)} w d^3x$ as the thermal-averaged w (assumed to be equal to the thermal top ascent rate w_t) in (4), using the product rule $d(w_tV)/dt = Vdw_t/dt + w_t dV/dt$, dividing by thermal volume V, and rearranging terms, we express the thermal-averaged momentum budget as

$$\rho_0\frac{dw_t}{dt} = -F_d + E + \rho_0\overline{B}, \tag{5}$$

where $F_d \equiv V^{-1}\int_{\Omega(t)}(\partial p/\partial z)d^3x$ is the thermal-averaged pressure drag force, $E \equiv V^{-1}\int_{\partial\Omega(t)}(\hat{\mathbf{n}}\cdot\mathbf{u}_e)\rho_0 w d^2x - V^{-1}(dV/dt)w_t\rho_0$ is the momentum entrainment, and $\overline{B} \equiv V^{-1}\int_{\Omega(t)}B d^3x$ is the thermal-averaged buoyancy. Equation (5) expresses the vertical momentum budget of a thermal as an acceleration term on the left-hand side and a drag force arising from vertical pressure gradients, an entrainment "pseudoforce," and a buoyant forcing term on the right-hand side.

We assume that detrainment is negligible and that thermal expansion incorporates fluid with $w = 0$. Thus, net entrainment is related only to the change in thermal volume (following the Boussinesq approximation). This assumption is well justified based on the DNS of dry thermals from LJ2019; see Morrison et al. (2022) for further discussion. It follows that we can write the entrainment term as $E \approx -V^{-1}(dV/dt)w_t\rho_0$, where $V^{-1}(dV/dt) = (d\ln V/dz_t)w_t = \epsilon w_t$ using the chain rule. Thus, we can express $E \approx -\epsilon w_t^2\rho_0$.

We nondimensionalize the thermal momentum equation next. Based on a characteristic background fluid density ρ_0, thermal radius R_0, and thermal buoyancy B_0, we can define various scales including time $t_0 = \sqrt{R_0/B_0}$, velocity $w_0 = \sqrt{R_0B_0}$, and pressure $p_0 = \rho_0B_0/R_0$. From this, we write $t^* = t/t_0$, $z^* = z/R_0$, $w^* = w/w_0$, $F_d^* = (R_0/p_0)F_d$, $E^* = E/E_0 = [R_0/(\rho_0w_0^2)]E$, and $B^* = B/B_0$. Substituting these relations into the thermal-averaged momentum budget gives a nondimensional form of the equation:

$$\frac{\rho_0w_0^2}{R_0}\frac{dw_t^*}{dt^*} = -\frac{p_0}{R_0}F_d^* + \frac{\rho_0w_0^2}{R_0}E^* + \rho_0B_0\overline{B}^*. \tag{6}$$

Multiplying (6) by $R_0/(w_0^2\rho_0)$, it can be expressed in terms of two nondimensional flow parameters: Froude number $F_r = w_0^2/(B_0R_0)$ and Euler number $E_u = p_0/(\rho_0w_0^2)$. This gives

$$\frac{dw_t^*}{dt^*} = -E_uF_{pB}^* - E_uF_{pD}^* + E^* + F_r^{-1}\overline{B}^*, \tag{7}$$

where the nondimensional drag force F_d^* is divided into two parts following the standard separation of perturbation pressure into buoyant and dynamic components: $F_d^* = F_{pB}^* + F_{pD}^*$. The buoyant part is approximated by $E_uF_{pB}^* \approx F_r^{-1}(1 - C_v)\overline{B}^*$. The term C_v is a virtual mass parameter defined such that the sum of $F_r^{-1}\overline{B}^*$ and $-E_uF_{pB}^*$ is equal to $F_r^{-1}C_v\overline{B}^*$. C_v depends on the structure of the buoyancy field. For example, $C_v = 2/3$ for a spherical buoyancy perturbation (Tarshish et al. 2018). It follows that the nondimensional effective buoyancy—the sum of buoyancy and buoyant perturbation pressure forcing—is $B_{\mathrm{eff}}^* = C_v\overline{B}^*$.

We approximate the dynamic pressure part of thermal drag using the standard drag equation divided by V to give a volume-averaged dynamic pressure drag force: $F_{pD} = \rho_0 w_t^2 C_d A/(2V)$, where A is the cross-sectional thermal area perpendicular to the flow. Defining γ as the ratio AR/V, which is a constant for self-similar thermals ($\gamma = 3/4$ for a spherical thermal), we can express the thermal-averaged nondimensional dynamic pressure drag force as $F_{pD}^* = w_t^{*2}\gamma C_d/(2R^*)$. Note that $C_d \approx 0$ for initially spherical ($A_r = 1$) dry buoyant thermals (Morrison et al. 2022). Although C_d could in principle vary with A_r, the thermal simulations presented in section 4, with A_r varying from 0.5 to 2, all have small C_d (magnitude less than 0.1). Thus, the dynamic pressure drag is relatively unimportant in the thermal momentum budget. Nonetheless, we retain this term and C_d in the equations for generality.

Hereinafter, we take characteristic values of the physical scales ρ_0, R_0, and B_0 as unity so that $F_r = 1$ and $E_u = 1$ and drop the * indicating nondimensional quantities for convenience. It follows that we can write the nondimensional thermal-averaged vertical momentum budget equation given by (7) as

$$\frac{1}{2}\frac{dw_t^2}{dz_t} + w_t^2\epsilon + \frac{\gamma C_d w_t^2}{2R} - C_v\overline{B} = 0, \tag{8}$$

where we have used the above relations for E and buoyant and dynamic pressure contributions to drag, and the chain rule to express the time derivative as a height derivative following the thermal top: $d/dt = w_t d/dz_t$ (z_t is the thermal top height).

If we assume $\alpha \equiv dR/dz_t$ is constant, consistent with recent numerical modeling studies (Morrison et al. 2021; LJ2019) and the simulations herein, we can write $R = R_0 + \alpha z_t = 1 + \alpha z_t$ by integrating α from $z_t' = 0$ to $z_t' = z_t$. Also, $\overline{B} = B_0/R^3 = 1/R^3$ (since we take $B_0 = 1$ as the initial buoyancy scale, and $\overline{B}$ scales inversely with the change in thermal volume as the thermal entrains nonbuoyant environmental fluid and expands) and $\epsilon = e/R$ (LJ2019). With these assumptions and relations, (8) may be written as

$$\frac{1}{2}\frac{dw_t^2}{dz_t} + \left(e + \frac{\gamma C_d}{2}\right)\frac{w_t^2}{(1+\alpha z_t)} - \frac{C_v}{(1+\alpha z_t)^3} = 0. \tag{9}$$

Assuming α, e, C_v, γ, and C_d are constants, (9) represents a first-order linear differential equation with an exact solution given by

$$w_t^2 = \frac{C_v}{\left(e - \alpha + \frac{\gamma}{2}C_d\right)(1+\alpha z_t)^2} + k_1(1+\alpha z_t)^{-(2e/\alpha)-(\gamma C_d/\alpha)}, \tag{10}$$

where k_1 is a constant of integration. Given the boundary condition $w_t = 0$ at $z_t = 0$, we may solve for k_1 and use this in (10) to give

$$w_t^2 = \frac{C_v}{\left(e - \alpha + \frac{\gamma}{2}C_d\right)(1+\alpha z_t)^2} - \frac{C_v}{\left(e - \alpha + \frac{\gamma}{2}C_d\right)(1+\alpha z_t)^{(2e/\alpha)+(\gamma C_d/\alpha)}}. \tag{11}$$

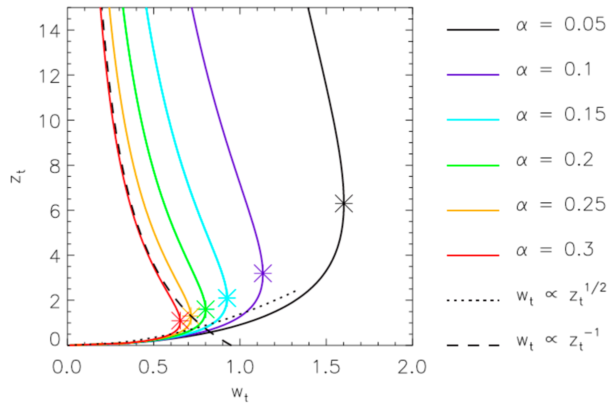

FIG. 2. Analytic solutions to the thermal w_t Eq. (11) as a function of nondimensional thermal top height z_t. Different color lines indicate assumed values of thermal expansion rate α as labeled. Black dotted and dashed black lines illustrate scalings from the asymptotic analysis corresponding to the "slippery" regime during thermal spinup and "sticky" regime after spinup, respectively. The * symbols indicate the height and magnitude of maximum w_t for each curve.

Equation (11) is similar to Escudier and Maxworthy [1973, Eqs. (9)–(11) therein], except that we invoke the Boussinesq approximation, express w_t using a single analytic equation as a function of height z_t rather than t, and include an explicit dependence on α.

Solutions for w_t can be obtained from (11), provided values of α, e, γ, C_d, and C_v are known. Past literature has suggested $\alpha \sim 0.05$–0.3 (Lai et al. 2015), $e \approx 3\alpha$ (LJ2019), $C_d \approx 0$ (Morrison et al. 2022), meaning that γ is not relevant, and $C_v \sim 0.5$–0.8 (Tarshish et al. 2018). Examples of solutions to the analytic w_t Eq. (11) using $e = 3\alpha$, $C_d = 0$, $C_v = 2/3$, and α ranging from 0.05 to 0.3 are shown in Fig. 2 (solid lines). With these parameter values, (11) gives a family of solutions that all exhibit a sharp increase of w_t with height initially corresponding to a "slippery" regime when upward buoyant forcing is primarily balanced by vertical acceleration, followed by a slower decrease of w_t corresponding to a "sticky" regime when weak buoyant forcing is balanced mainly by entrainment.[2] This shape of the w_t profile with the two distinct regimes of thermal evolution was discussed previously via analysis of numerical solutions (e.g., Wang 1971; Tarshish et al. 2018). In subsequent sections, we will determine constraints on values of α while also briefly exploring how e and C_v vary with the initial thermal aspect ratio.

We can understand scaling behaviors in the slippery and sticky regimes via asymptotic analysis and expansion of (11), similar to the asymptotic analysis of Escudier and Maxworthy (1973) applied to their equation set for w_t. For the slippery regime when $z_t < 1$, we can expand (11) using Taylor series

[2] Note that the sticky regime is primarily a balance between entrainment and buoyant forcing for dry thermals, whereas Romps and Charn (2015) identified a sticky regime for cloud thermals consisting mainly of a balance primarily between buoyant forcing and downward pressure gradient forcing.

about $z_t = 0$ and retain the first-order term to give $w_t \propto z_t^{1/2}$. This is equivalent to a scaling of $z_t \propto t^2$ since $w_t = dz_t/dt$, which is consistent with the theory and numerical simulations in the slippery regime from Tarshish et al. (2018).

In contrast, when $z_t \gg 1$ for the sticky regime, $1 + \alpha z_t \approx \alpha z_t$ and the second term on the right-hand side of (11) is negligible compared to the first term (for $2e/\alpha + \gamma C_d/2 > 2$, which is satisfied for typical values of $2e/\alpha \approx 6$ and $\gamma C_d \approx 0$), implying a scaling of w_t with z_t^{-1}. This is equivalent to a scaling of $z_t \propto t^{1/2}$, consistent with the theory and simulations of LJ2019 for the sticky regime. These scaling regimes well correspond to full solutions of the analytic w_t equation, Eq. (11), for small and large z_t as seen in Fig. 2 and are also consistent with the asymptotic analysis from Escudier and Maxworthy (1973).

b. *Impulse, circulation, and thermal spreading rate*

Although (11) accounts for the impact of thermal spreading rate α on w_t via entrainment, by itself it does constrain α. However, the thermal momentum budget can provide a basic constraint on α via the impulse–circulation relation (e.g., Turner 1957; Lai et al. 2015; McKim et al. 2020; Morrison et al. 2021). A thermal's circulation Γ can be calculated as the integral of velocity along a circuit ∂S passing through the thermal center and returning through the ambient fluid or equivalently as an area integral of vorticity over a region S bounded by the circuit ∂S. If we assume axisymmetry, this area integral can be expressed as the integral of azimuthal vorticity ω_ϕ over S in axisymmetric (r, z) coordinates (McKim et al. 2020):

$$\Gamma = \oint_{\partial S} \mathbf{u} \cdot d\mathbf{l} = \int_S \omega_\phi \, dr\, dz. \tag{12}$$

The time rate of change of circulation is given by

$$\frac{d\Gamma}{dt} = \int_S -\frac{\partial B}{\partial r}\, dr\, dz = \int_{z_{\rm bs}}^{z_{\rm ts}} B_c \, dz \tag{13}$$

for an inviscid fluid, where B_c is the buoyancy along the thermal's vertical axis, $z_{\rm bs}$ and $z_{\rm ts}$ are the bottom and top heights of region S, and the region with $B_c > 0$ is assumed to be encompassed within S (hereinafter when writing this integral, we drop the limits $z_{\rm bs}$ and $z_{\rm ts}$ for convenience). In words, (13) shows that the rate of increase in Γ during spinup is equal to the vertical integral of core buoyancy.

We can directly relate Γ to α via the impulse–circulation relation. Fluid impulse I is the total momentum change starting from rest caused by external forcing over a finite region of space. For an idealized infinite domain in the absence of nonconservative forces and applying the incompressible Boussinesq approximation, I is related to vorticity ω by (e.g., Batchelor 2000)

$$I = \frac{\rho_0}{2}\int_{\mathcal{V}} \mathbf{x} \times \omega d^3x, \tag{14}$$

where $\mathcal{V}$ is the entire domain and $\mathbf{x}$ is a position vector. The term I is essentially a record of the volume- and time-integrated external (here, gravitational via a localized buoyancy anomaly) forcing on the fluid. If the region of nonzero vorticity within the domain is concentrated on a circle with a radius equal to R_v (i.e., the vortex ring radius, see Fig. 1), and this region of vorticity is small compared to R_v, then (14) can be approximated using the second part of (12) as (Turner 1957; McKim et al. 2020)

$$I_z = \pi\rho_0\Gamma R_v^2. \tag{15}$$

The subscript "z" indicates that the impulse is only in the z direction as a consequence of the axisymmetry of the flow.

Taking d/dt of (15), we have

$$\frac{dI_z}{dt} = \pi\rho_0\left(R_v^2\frac{d\Gamma}{dt} + \Gamma\frac{dR_v^2}{dt}\right) = F_B, \tag{16}$$

where F_B is the domain-integrated buoyant forcing, which is constant in time following (3) in a neutrally stable environment.

Equation (16) can be directly related to α using the chain rule $d/dt = w_t d/dz_t$ to give $dR_v^2/dt = \zeta^2 dR^2/dt = 2\zeta^2 R w_t \alpha$, where ζ is the ratio of the vortex radius to the thermal radius and assumed to be constant following self-similarity but may vary with A_r. Substituting this relation for dR_v^2/dt in (16) and substituting (13) for $d\Gamma/dt$, we have

$$\pi\rho_0\zeta^2R^2\int B_c\, dz + 2\pi\rho_0\Gamma\zeta^2 R w_t\alpha = F_B. \tag{17}$$

The physical interpretation of (13)–(17) is that if there is no buoyancy along the thermal's vertical axis ($B_c = 0$), then there is no change in the thermal's circulation with time ($d\Gamma/dt = 0$) and the first term on the left-hand side of (17) is zero. The removal of buoyancy along the thermal's vertical axis by the upward encroachment of nonbuoyant environmental fluid entrained from below the thermal corresponds to the point of thermal spinup. With $F_B > 0$, $B_c = 0$ implies $\alpha > 0$ in the second term since ζ, R, and w_t are all >0. This is consistent with the basic argument from Turner (1957) and McKim et al. (2020) explaining how the impulse–circulation relation dictates a positive thermal expansion rate when $d\Gamma/dt = 0$ and $F_B > 0$. Moreover, F_B is constant as noted above, and self-similarity implies α and ζ are constants and $R \propto z_t$. This gives $w_t \propto z_t^{-1}$, which is consistent with the scaling from our analytic w_t equation, Eq. (11), in the "sticky" regime where $z_t \gg 1$. During the spinup phase corresponding to the "slippery" regime, $B_c > 0$ and the first term on the left-hand side of (17) > 0. This implies that the second term on the left-hand side of (17) must be smaller before spinup than after.

If Γ is known when the thermal is spun up, we can derive an analytic expression for α by combining (15) and (17) with the relation between a thermal's impulse and w_t (Akhmetov 2009; McKim et al. 2020): $I_z = mR^3\rho_0(1 + C_v)w_t$, where m is a shape parameter equal to the ratio of thermal volume to R^3. This is analogous to Eq. (17) in McKim et al. (2020), who expressed e (rather than α) in terms of ζ, F_B, Γ, C_v, and m. All of these parameters likely depend on A_r. For example, the virtual mass coefficient C_v depends on the thermal shape (Tarshish et al. 2018), while Γ (after spinup) has a strongly nonlinear dependence on A_r as we show in section 4 from the thermal numerical simulations. Such dependencies are broadly consistent

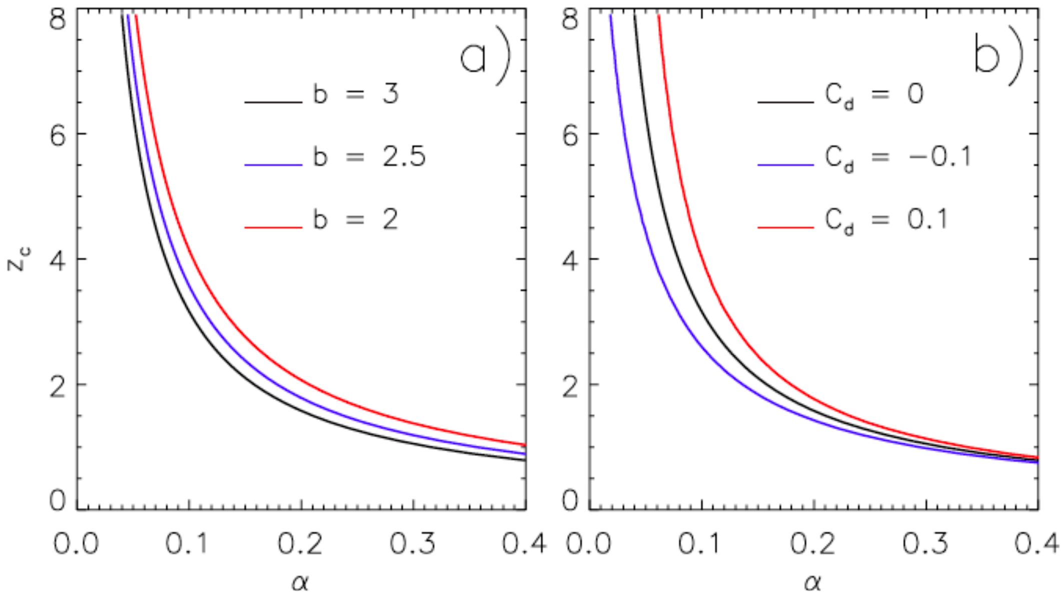

FIG. 3. Solutions to the analytic α–z_c relation (18) with (a) $C_d = 0$ and varying b as indicated and (b) $b = 3$ and varying C_d as indicated.

with sensitivity of α to A_r but complicate the interpretation and explanation of this sensitivity.

These complications motivate an alternative approach described below that relates α to the thermal top height when spinup is achieved, corresponding to the thermal top height when w_t reaches its maximum. This is in a similar vein as relating α (or e) to ζ, F_B, Γ, C_v, and m, but with much simpler functional dependencies allowing for a clear understanding of the variation of α with A_r.

c. *Relationship between thermal spinup height and spreading rate* α

We define a critical thermal top height z_c separating the "slippery" and "sticky" regimes when $dw_t/dz_t = 0$ and w_t is a maximum. During spinup, $dw_t/dz_t > 0$ as $d\Gamma/dt > 0$ owing to the presence of buoyant fluid along the thermal's vertical axis. After buoyancy is eroded along the thermal's vertical axis from entrainment of environmental fluid, Γ is constant following (13), and thus, $dw_t/dz_t < 0$ following the $w_t \propto z_t^{-1}$ scaling implied by (17). Taken together, the implication is that z_c corresponds to the thermal top height at the time when core buoyancy is eroded and thereafter $d\Gamma/dt \approx 0$, which is supported by the numerical simulations presented in section 4.

The critical height z_c is obtained by taking d/dz_t of (11) and setting $dw_t/dz_t = 0$. We also introduce the parameter $b \equiv e/\alpha$, the ratio of entrainment efficiency to thermal spreading rate. The resulting expression is solved analytically to yield the following relation between z_c, α, b, γ, and C_d:

$$\left(b + \frac{\gamma C_d}{2\alpha}\right)(1 + \alpha z_c)^{-2b-(\gamma C_d/\alpha)+2} = 1. \tag{18}$$

Figure 3 shows α calculated from (18) as a function of z_c for b equal to 2, 2.5, and 3 and $C_d = 0$ (Fig. 3a) and for C_d equal to −0.1, 0, and 0.1 and $b = 3$ (Fig. 3b). For these calculations, $\gamma = 3/4$ corresponding to spherical thermals for simplicity. A self-similar thermal shape implies $b = 3$, meaning that $e = 3\alpha$ and $\epsilon \equiv d(\ln V)/dz_t = 3\alpha/R$ (LJ2019). Deviations from $b = 3$, therefore, indicate the degree to which thermals are not self-similar. Zhao et al. (2013), while noting self-similarity of gross thermal characteristics (overall thermal shape and size) after spinup, found that internal vorticity and density structures evolved nonsimilarly in their experimental study. In the simulations presented later in the current paper, b is somewhat smaller than 3, ranging from ~2.4 to 2.7 for $A_r < 2$. For the $A_r = 2$ simulation, $b \sim 2.1$, indicating that initially vertically elongated thermals change their shape relatively more than the smaller A_r thermals. This may be related to the inability of thermals to take in all initially buoyant fluid when $A_r \geq 2$, leaving a wake of buoyant fluid below the thermal, as discussed in Lai et al. (2015). Nonetheless, sensitivity of α to b over the range of 2–3 is fairly small, with a 24% decrease in α as b is increased from 2 to 3.

The change in α for a given z_c as C_d is varied from −0.1 to 0.1 is small in magnitude, with α varying by up to 0.04 for the range of parameters shown in Fig. 3b. The relative change is greatest at small values of α (large z_c), up to ~50% in Fig. 3b. For the thermal numerical simulations detailed later in the paper, with A_r varying from 0.5 to 2, mean C_d ranges from −0.06 to 0.08 [using the same method to calculate C_d from the simulated dynamic perturbation pressure field as in Morrison et al. (2022)]. Thus, dynamic pressure drag is relatively unimportant in (18), and hereinafter, we will assume $C_d = 0$. With this assumption, (18) can be rearranged to give

$$\alpha = \frac{b^{1/(2b-2)} - 1}{z_c}. \tag{19}$$

If we further assume a self-similar thermal shape, we can use (19) with $b = 3$ to obtain

$$\alpha = \frac{3^{1/4} - 1}{z_c}. \quad (20)$$

The one-to-one relationship between α and z_c means that if z_c is known, this uniquely constrains the value of α. We emphasize that z_c does not *cause* a particular value of α, but if z_c is known, then α can be predicted from it. A key point is that the expressions for α in (18)–(20) are independent of C_v and thus expected to have little dependence on A_r (given that b does not vary much with A_r and $C_d \approx 0$). Equation (20) gives consistent results with the analytic thermal w_t profiles shown in Fig. 2, which have z_c ranging from ~1 to 6 for α of 0.05–0.3 (for $b = 3$ and $C_d = 0$).

d. Relationship between z_c and A_r

As argued in the previous subsection, z_c corresponds to the thermal top height when buoyant fluid along the thermal's vertical axis is replaced by entrained environmental fluid (meaning circulation is approximately constant thereafter). This erosion of buoyancy in the thermal core occurs as nonbuoyant parcels are entrained near the thermal bottom and move upward relative to the thermal as a whole. Thus, we expect the time scale for loss of buoyancy along the thermal's vertical axis to be equal to the time for parcels entrained near the thermal bottom to travel upward through the thermal.

A parcel must travel a distance of the initial thermal depth plus z_c to ascend through the thermal in the same amount of time as the thermal top takes to reach height z_c. Since we can express the initial thermal depth as $D_0 = 2A_r$ (keeping in mind $R_0 = 1$), this time scale is

$$\tau_c = \frac{z_c + 2A_r}{\overline{w_p}}, \quad (21)$$

where $\overline{w_p}$ is the time-averaged parcel vertical velocity along its Lagrangian path: $\overline{w_p} \equiv \tau_c^{-1}\int_0^{\tau_c} w_p(t)dt$. By definition, this is the same time scale for the thermal top to reach z_c (starting from $z_t = 0$), implying

$$\tau_c = \frac{z_c}{\overline{w_t}}, \quad (22)$$

where $\overline{w_t} \equiv \tau_c^{-1}\int_0^{\tau_c} w_t(t)dt$ is the time-averaged thermal top vertical velocity.

Substituting (21) in (22) and solving for z_c gives

$$z_c = \frac{2A_r}{\sigma - 1}, \quad (23)$$

where $\sigma \equiv \overline{w_p}/\overline{w_t}$ is the ratio of the time-averaged vertical velocities of the parcel and thermal top.

Equation (23) can be combined with (19) to yield an expression for α as a function of A_r:

$$\alpha = \frac{\left(b^{1/(2b-2)} - 1\right)(\sigma - 1)}{2A_r}. \quad (24)$$

If we take $b = 3$ following self-similarity, this gives

$$\alpha = \frac{(3^{1/4} - 1)(\sigma - 1)}{2A_r}. \quad (25)$$

e. Predicting σ from Hill's analytic spherical vortex

The thermal aspect ratio A_r is specified from the initial conditions, leaving σ as the only unknown parameter in (25) to obtain α. This parameter is closely related to the thermal internal flow structure, which controls the rate of parcel ascent in the thermal core relative to the thermal as a whole. Lai et al. (2015) noted similarity of the flow structure of thermals to Hill's vortex, particular for $A_r = 2$. They found that the analytic Hill's vortex solution deviated more from numerical thermal simulations for smaller A_r, but noted "it can still give a fair prediction of flow field" for A_r as low as 0.5. In agreement with Lai et al. (2015), in section 4, we show a close correspondence of vertical velocity profiles along the central axis in numerically simulated thermals to Hill's vortex for initial A_r of 1 and 2, with more deviation but still fairly similar w profiles for $A_r = 0.5$.

Given the overall similarity of Hill's analytic vortex with the internal flow of thermals, we can approximate σ from the vertical profile of w in the core of Hill's vortex. The w field within Hill's vortex is given by

$$w(r, z) = -\frac{3W}{4}\left[4\left(\frac{r}{a}\right)^2 + 2\left(\frac{z}{a}\right)^2 - \frac{10}{3}\right], \quad \sqrt{z^2 + r^2} \le a, \quad (26)$$

in axisymmetric coordinates, where a is the vortex radius and W is the steady vortex ascent rate. The flow outside of the vortex is given by

$$w(r, z) = \frac{Wa^3(2z^2 - r^2)}{2(z^2 + r^2)^{5/2}}, \quad \sqrt{z^2 + r^2} > a. \quad (27)$$

Along the vertical axis ($r = 0$), the w profile is symmetric and features an increase in the bottom half of the vortex, a maximum w equal to $5/2W$ at $z = 0$, and a decrease in the upper half.

A parcel initially at the bottom of Hill's vortex will rise at the same rate as the vortex since $u = 0$ and $w = W$ at this location (i.e., it is a stagnation point in the vortex-relative flow). However, a parcel initially just above the vortex bottom at $r = 0$ will rise relative to the vortex as a whole. Thermals, owing to their buoyancy, entrainment, and nonsteady behavior, do not have such stagnation points, and parcels initiated at the thermal bottom rise through the thermal depth as demonstrated by the simulations in section 4. Thermal flow is similar to Hill's vortex in the interior. Thus, although parcel ascent differs between thermals and Hill's vortex near the top and bottom boundaries, it is similar in the interior with an acceleration toward the center followed by a deceleration above.

Because of the stagnation points in Hill's vortex, we cannot use it directly to estimate the Lagrangian time scale for parcel ascent starting from the thermal bottom. However, given similarity of the interior flow between thermals and Hill's vortex, a rough approximation is to replace the Lagrangian time-mean w along the parcel's path with the Eulerian vertical-mean w from Hill's vortex: $\overline{w_p} \approx (2a)^{-1}\int_{z=-a}^{z=a} w(z)dz = 2W$, where $w(z)$ is from (26) with $r = 0$. This gives $\sigma = \overline{w_p}/W \approx 2$, which is expected to be an upper estimate since the Lagrangian mean weights toward smaller values of w compared to the Eulerian mean. Additional context for this approach is provided by analysis of the thermal numerical simulations. Comparing the Lagrangian mean $\overline{w_p}$ for a parcel initiated at the thermal bottom versus the time-averaged Eulerian mean w (from thermal bottom to top) during the spinup period shows a close correspondence between the two, with relative differences ranging from -6% to 14%. Furthermore, σ values from the simulations generally range from 1.80 to 1.95 (with the exception of $\sigma \approx 1.63$ in the $A_r = 2$ simulation), close to but slightly less than $\sigma = 2$.

We can also calculate $\overline{w_p}$ from Hill's vortex exactly for a parcel initiated *above* the vortex bottom and ending the same distance below vortex top. This is obtained from

$$\overline{w_p} = (D + 2fa)/\Delta t, \tag{28}$$

where f is the fractional distance from the vortex center ($z = 0$) where the parcel is initiated relative to its radius a, Δt is the time for the parcel to travel along this path, and $D = W\Delta t$ is the distance traveled by the vortex as a whole over Δt. The distance $D + 2fa$ is the total distance traveled by the parcel over its Lagrangian path. Following a trajectory along $r = 0$, $dz/dt = w(z) - W$, where z is height relative to the ascending vortex and $w(z) - W$ is the vortex-relative parcel velocity. The time scale for ascent is calculated as $\int_{t=0}^{t=\Delta t} dt = \Delta t = \int_{z=-fa}^{z=fa} [w(z) - W]^{-1}\, dz$. The integral on the right-hand side can be solved analytically by substituting (26) for $w(z)$ combined with $r = 0$ to yield

$$\Delta t = -\frac{2a}{3W}[\ln(1 - f) - \ln(1 + f)]. \tag{29}$$

Combining (28) and (29) with $D = W\Delta t$ gives an expression for $\overline{w_p}$, and σ is then obtained by dividing this expression by W to give

$$\sigma = 1 - 3f[\ln(1 - f) - \ln(1 + f)]^{-1}. \tag{30}$$

A parcel initiated just above the vortex bottom, with f of 0.99–0.9 (i.e., initiated at a distance of 0.01–0.1 radii above the thermal bottom and ending the same distance below top), gives σ of 1.6–1.9 consistent with the simulations.

Following discussion in Lai et al. (2015), the flow field of the Norbury vortex family (Norbury 1973), which generalizes Hill's vortex to variable ring vortex thickness, may be closer to the thermal simulations with varying A_r. Similarly, the O'Brien (1961) analytic spheroidal vortex model might give a better description of the flow for spheroidal thermals. However, these models are steady state and also have stagnation points. Since Hill's vortex provides a reasonable description of the interior thermal flow over a range of A_r, we use it to constrain σ following the discussion above.

Combining $\sigma \approx 2$ from the Eulerian mean w of Hill's vortex with (19) and (23) gives our final theoretical expression for α (with the assumption of self-similarity so that $b = 3$):

$$\alpha \approx \frac{(3^{1/4} - 1)}{2A_r} \approx \frac{0.158}{A_r}. \tag{31}$$

3. Description of the numerical simulations

a. Model description and experimental design

We utilize the Cloud Model 1 (CM1) fluid flow model to numerically simulate thermals with varying initial A_r. CM1 is a nonhydrostatic model which has been widely used to simulate idealized atmospheric flows. Here, we use the incompressible Boussinesq configuration to solve the filtered Navier–Stokes equations similar to the large-eddy simulation (LES) configuration in Morrison et al. (2022). Prognostic variables are the 3D components of flow velocity and potential temperature perturbation θ', although near-axisymmetry of the model fields is retained. Buoyancy B is obtained by $g\theta'/\theta_0$, where θ_0 is a constant background θ of the fluid environment. As noted by Morrison et al. (2022), in this framework, prognosing θ' is equivalent to prognosing B itself. Simulations are nondimensionalized using a length scale equal to the radius of the initial thermal R_0 (the radius of the initial buoyancy perturbation) and a time scale given by $\sqrt{R_0/B_0}$, where B_0 is the initial thermal buoyancy. The density scale ρ_0 is equal to the constant background fluid density in this Boussinesq framework. All other quantities are nondimensionalized following these basic scales.

The initial A_r of thermals is varied from 0.5 to 2, similar to the range from Lai et al. (2015). As we show in section 4, this produces a wide spread of α (~0.08–0.25). Thermals are initiated by adding a buoyancy perturbation B_0 uniformly within a spheroidal volume having a horizontal radius of R_0 and a vertical radius of A_rR_0. To minimize the impacts of boundary conditions, the initial buoyancy perturbations are centered at a height of $4R_0$, and the horizontal domain width is $\geq 16R_0$ and the vertical domain height is $64A_rR_0$ (64 times the initial vertical thermal radius). The model grid is isotropic in all three directions with a grid spacing ΔL_m equal to $0.1A_rR_0$. Since the initial A_r varies from 0.5 to 2, ΔL_m ranges from $0.05R_0$ to $0.2R_0$. The time step is 0.0362 times the time scale $\sqrt{R_0/B_0}$. Because the thermals expand as they ascend, the overall dynamical structure is well resolved with at least 10 grid points horizontally and 20 points vertically across the thermals. An additional set of simulations with A_r varying from 0.5 to 2 but $\Delta L_m = 0.1R_0$ (thus at least 20 points horizontally and 10 points vertically across the thermals) was also run and analyzed. This set gives similar results to the first set, and thus, we only report the results of the first set of simulations in this paper. Other details of the model setup are given in Table 1.

In this study, we use LES applied to the filtered Navier–Stokes equations instead of DNS to retain a close connection to atmospheric modeling, particularly modeling of dry and moist thermals in the planetary boundary layer and

TABLE 1. Configuration details for the CM1 simulations presented in this paper.

Feature	Configuration
Dynamics	Incompressible Boussinesq
Number of horizontal grid points	320 × 320
Number of vertical grid points	640
Advection	Fifth-order WENO
Subgrid-scale mixing	Smagorinsky type
Lateral boundary conditions	Periodic
Lower and upper boundary conditions	Free slip and rigid

convective clouds in which DNS is not possible given the huge $O(10^9)$ Reynolds numbers involved. The LES framework is also consistent with our previous work on dynamic drag of dry buoyant thermals (Morrison et al. 2022) and similar to previous thermal simulations of Lai et al. (2015). The subgrid-scale (SGS) mixing follows a Smagorinsky-type approach as implemented by Stevens et al. (1999, see their appendix B, section b). The SGS mixing length is set to ΔL_m. Because the dissipation scale (the model's filter scale) is a relatively large fraction of the thermals' radii, the resolved scale flow is smooth and thus appears laminar. The resulting thermal evolution and internal flow structure of the simulated thermals is remarkably similar to the DNS of initially spherical laminar thermals in LJ2019 ($R_e = 630$). Results across the range of A_r are close to those of Lai et al. (2015), who also numerically solved the filtered (discretized) Navier–Stokes equations but using a k–δ turbulence closure (Launder and Spaulding 1974), where k is the resolved kinetic energy and δ is the energy dissipation rate. Our simulations are integrated forward in time until the thermal top (as defined in section 3b) reaches a height of $15R_0$ above the initial thermal top (i.e., top of the initial buoyancy perturbation). To investigate the internal thermal flow characteristics, particularly the time for ascent of a parcel through the thermal, each simulation includes forward trajectories for a parcel placed at the thermal bottom at the initial time. We use the built-in parcel trajectory calculations in CM1 which are done during the model integration using linear interpolation of the flow field at each model time step.

b. Analysis methodology

Thermal boundaries must first be identified and tracked in order to analyze thermal behavior including spreading rate. We use a method similar to LJ2019 and Morrison et al. (2022). At each output time (at an interval of 0.542 times the time scale $\sqrt{R_0/B_0}$), the horizontal thermal midpoint is determined by the column with maximum vertically integrated pressure perturbation. Thermal top is defined by the buoyancy field analogously to LJ2019: the provisional thermal top height z_t is calculated as the highest level where the horizontally averaged $B \geq 1/10$ of the maximum horizontally averaged B (maximum defined in the vertical). This is done at each output time to generate a time series of provisional z_t, from which we calculate the thermal top ascent rate w_t using a centered difference in time. Using z_t obtained directly from the B field can result in noise in w_t and hence in thermal volume and radius. However, unlike LJ2019 and Morrison et al. (2022), we apply this w_t directly to calculate the streamfunction and thermal boundaries rather than using a fitting procedure to the analytic scaling relation $w_t \propto t^{-1/2}$ (or analogously, $w_t \propto z_t^{-1}$) from similarity theory. Although the fitting method reduces noise, it is only applicable in the sticky regime after spinup, and we are interested in thermal behavior both during spinup and after. Although w_t here is somewhat noisy, the spreading behavior of thermals and its sensitivity to A_r are clear.

Once w_t is determined, model output is azimuthally averaged around the horizontal midpoint using a radial–vertical grid (r, z) with the same grid spacing as the original Cartesian grid. We then calculate the Stokes streamfunction using the thermal-relative flow field. This is done by integrating

$$\frac{\partial \psi}{\partial r} = 2\pi r(w_{\text{axi}} - w_t), \tag{32}$$

$$\frac{\partial \psi}{\partial z} = -2\pi r u_{\text{axi}}, \tag{33}$$

where u_{axi} and w_{axi} are the regridded radial and vertical velocities in cylindrical coordinates, with the boundary condition $\psi(r = 0, z = z_t) = 0$. The boundary of the thermal is the $\psi = 0$ contour. Thermal radius R is calculated as the widest region with $\psi \geq 0$. Spreading rate α is calculated from $\alpha = dR/dz_t$ using centered finite differencing. Fractional entrainment rate ϵ is calculated from $d(\ln V)/dz_t$, where V is defined by the volume with $\psi \geq 0$, again using centered finite differencing. Entrainment efficiency e is then obtained as the product of ϵ and R.

Other quantities of interest are 1) vorticity, which is calculated directly from the velocity field using centered finite differencing, and 2) buoyant and dynamic components of perturbation pressure, output directly from the model as described in Morrison et al. (2022).

4. Analysis of numerical simulations

Overall structure and evolution is similar for all of the simulated thermals. Starting from rest, rapid spinup ensues owing to vorticity generation from the thermals' buoyancy distributions. The thermals spread outward as they rise and entrain the surrounding fluid. Spinup of the thermals (after which circulation is nearly constant) occurs when a parcel initially placed at the thermal bottom rises to near proximity of the thermal top. Here, we calculate the critical height z_c as the thermal top height when spinup is achieved, rather than directly from the height where $dw_t/dz_t = 0$ and w_t is maximum because dw_t/dz_t is rather noisy. Nonetheless, z_c calculated from the parcel trajectories matches well with broad maxima in w_t as shown later.

In accordance with the theory presented in section 2, z_c ranges from about 1 to 6 as A_r is varied from 0.5 to 2 (Table 2). After spinup, when $z_t > z_c$ in the "sticky" regime, the thermals continue to expand by entraining environmental fluid, but their overall flow structure is fairly steady. The thermals undergo a

TABLE 2. Time-averaged $\alpha \equiv dR/dz_t$, $b \equiv e/\alpha$, virtual mass parameter C_v, ratio of parcel to thermal-time-averaged vertical velocity σ, circulation Γ, and critical spinup height z_c from the simulations with varying A_r. Note that b is obtained from the ratio of time-averaged e to time-averaged α. Because of some noise in calculating thermal velocity directly, σ is derived from (23) using z_c obtained from the simulations as described in the text. α, e, and C_v are calculated as time averages over the full simulation period, whereas Γ values are time-averaged after spinup to the end of the simulations.

A_r	α	b	C_v	σ	Γ	z_c
0.5	0.251	2.37	0.53	1.80	2.30	1.3
0.67	0.207	2.42	0.50	1.95	3.43	1.4
1	0.136	2.71	0.56	1.83	6.00	2.4
1.43	0.095	2.41	0.58	1.80	10.37	3.6
1.67	0.083	2.43	0.65	1.80	12.98	4.2
2	0.079	2.06	0.71	1.63	18.02	6.4

slow deceleration (relative to the faster acceleration during spinup) with w_t roughly proportional to $t^{-1/2}$ (and thus also proportional to z_t^{-1}) in accordance with the classical similarity theory of Scorer (1957).

Figure 4 shows vertical cross sections through the thermal center of B, w, horizontal vorticity in the y direction η_y, and streamfunction ψ after spinup, when thermal top height is at approximately $z_c + 2R_0$. Thermal flow features well documented by previous studies are seen in the figure. These include toroidal circulations with rotation centers near the thermal vertical midpoint, buoyancy concentrated near these rotation centers, and downward motion (in an absolute sense and relative to w_t) along the thermal periphery. Although buoyancy is almost entirely swept away from the thermal core (along the vertical axis at $X = 0$) for the $A_r = 0.5$ and 1 simulations, some positive buoyancy remains in the core when $A_r = 2$. There is also fluid with $B > 0$ and $\eta_y \neq 0$ below the thermal in this simulation (Figs. 4e,f). This occurs because not all of the initially buoyant fluid is taken into the thermal's vortex ring (toroidal circulation) when the aspect ratio is large, a result also noted by Lai et al. (2015). This behavior can be described by the "formation number" (Gharib et al. 1998), which is related to the maximum vorticity that can be incorporated into a vortex ring before it "pinches off" from a trailing stem. Earlier work showed a formation number of 4–5 for vortex rings (Gharib et al. 1998; Wang et al. 2009), whereas Lai et al. (2015) found a somewhat lower formation number of ~2, consistent with our results.[3] Despite the presence of a trailing stem of weakly buoyant fluid in the $A_r = 2$ simulation, buoyancy in the core is small relative to that near the rotation centers, and as detailed later, the theoretical relations between z_c, α, and A_r proposed in section 2 still well describe behavior of this simulation. We suspect that further increases in A_r would lead to greater deviation with the theory. Indeed, Lai et al. (2015) showed little change in α as A_r was increased beyond 2, likely because of the inability of such thermals to incorporate all of the initially buoyant fluid. The behavior of these thermals instead resembled a starting plume, consistent with the numerical results of Bond and Johari (2010).

Differences in thermal aspect ratio with varying initial A_r persist beyond spinup, although these differences are reduced compared to the initial A_r. The thermals with initial $A_r \geq 1$ become more flattened (smaller aspect ratio) during spinup. At the times shown in Fig. 4, the $A_r = 2$ simulation has an aspect ratio just slightly larger than 1, while that for $A_r = 1$ is about 0.75 and that for $A_r = 0.5$ is about 0.6. Different thermal aspect ratios among the simulations are reflected by variability in time-averaged values of C_v (virtual mass parameter, see section 2); see Table 2. Here, C_v is calculated at each model output time directly from the buoyancy and buoyant pressure forcing averaged over the thermal volume. Larger initial aspect ratios are associated with larger C_v, consistent with results from Tarshish et al. (2018). There is also an overall decrease in C_v over time during spinup as the thermals flatten, particularly for the simulations with $A_r > 1$. Changes in thermal shape during spinup also lead to deviation in b from the value for self-similar thermals ($b = 3$). The $A_r = 2$ thermal has the largest deviation, with $b \approx 2.06$, which is consistent with it experiencing the greatest change in aspect ratio during spinup, whereas b ranges from ~2.4 to 2.7 for the other simulations.

Thermal behavior during spinup is illustrated in Fig. 5, which shows vertical cross sections of B, w, η_y, and ψ in the same format as Fig. 4 except during the spinup period for the $A_r = 1$ simulation. Cross sections are shown in nondimensional time increments of 1.1 between $t = 1.6$ and 4.9. For context, the thermal top reaches z_c at $t \approx 3.7$. The basic mechanism of spinup is similar for all the runs. Consistent with the discussion in section 2d, entrainment occurs as environmental fluid is swept into the thermal from below in the convergent flow. This appears as a "bite" taken from the buoyancy field from below and occurs because thermal-relative vertical velocities are strongest in the thermal core. Baroclinic vorticity generation is concentrated along the edge of the buoyancy field where there are large horizontal buoyancy gradients. Once the buoyancy field is deformed and starts to wrap around the vortex core (i.e., the center of rotation), baroclinic generation and destruction of vorticity drives a spreading of the thermal in the manner outlined by McKim et al. (2020) and Morrison et al. (2021). Flattening of the thermal during spinup is also evident in Fig. 5.

In all simulations, the thermals' internal flow structures consist of thermal-relative ascent in the core, with strongest ascent along the vertical axis and descent along the periphery. This flow pattern strongly resembles Hill's analytic spherical vortex. To illustrate this point further, Fig. 6 compares w profiles along the thermals' vertical axis from the simulations with A_r of 0.5, 1, and 2 with w profiles at the vertical axis from Hill's vortex given by (26) and (27). This is similar to the comparison of w profiles from thermal simulations with Hill's vortex in Lai et al. (2015, Fig. 12 therein). Simulation results here are shown at the time of spinup when the thermal top is at z_c.

[3] Note that this difference may be explained in part because Gharib et al. (1998) defined formation number by the maximum vorticity incorporated into the vortex ring, while Lai et al. (2015) defined it by the maximum volume of fluid incorporated.

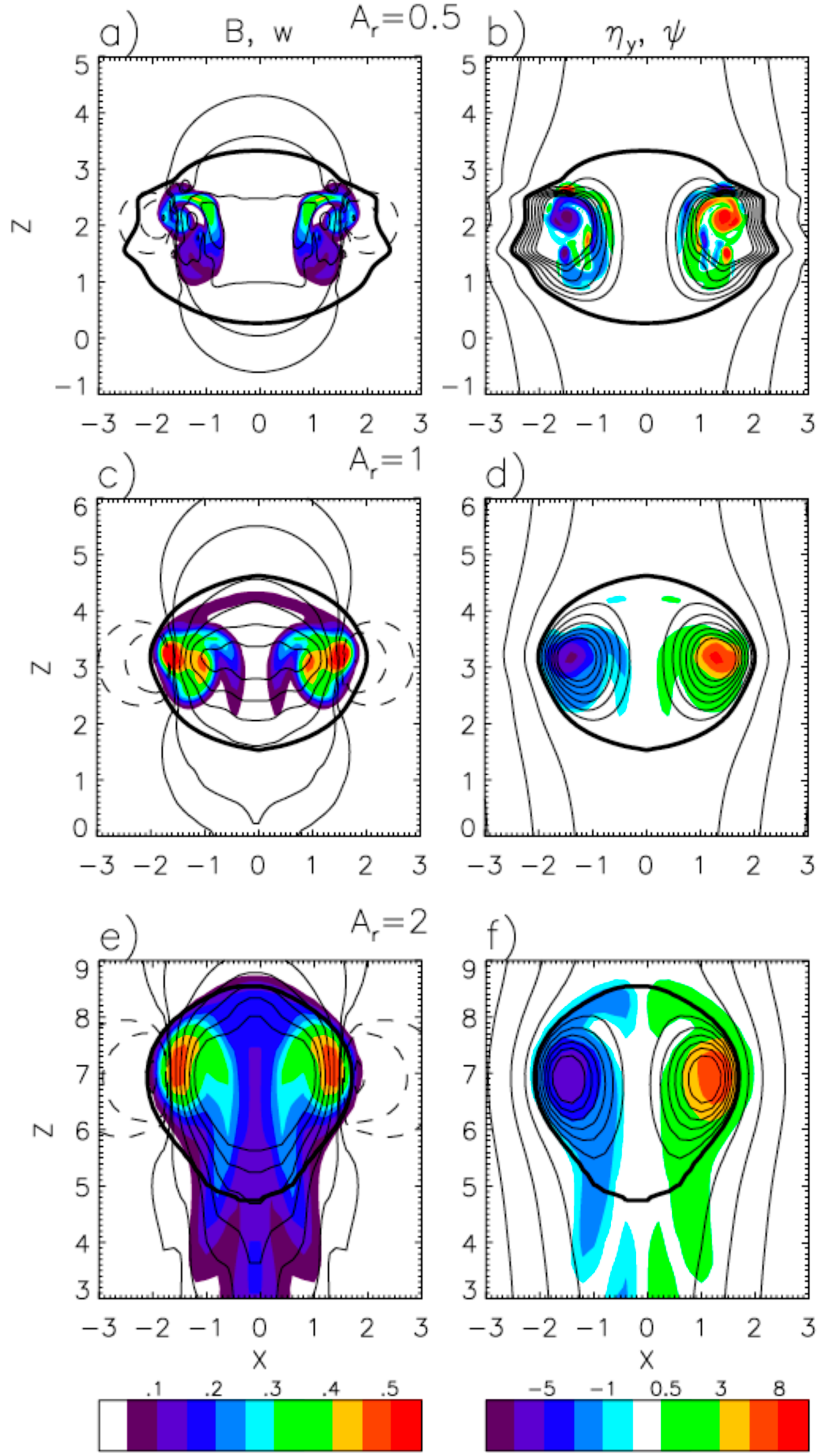

FIG. 4. Vertical cross sections of (left) buoyancy (color contours) and vertical velocity (thin black solid lines for positive w and thin black dashed lines for negative w; contour values are ±0.1, 0.2, 0.6, and every 0.4 thereafter); (right) vorticity in the y plane η_y (color contours) and streamfunction ψ (contour lines). Thick black lines show thermal boundaries defined by the $\psi = 0$ isoline. Results are shown for (a),(b) $A_r = 0.5$, (c),(d) $A_r = 1$, and (e),(f) $A_r = 2$. Cross sections are shown at times when the thermal top is approximately $2R_0$ above the critical height z_c for each simulation (see text).

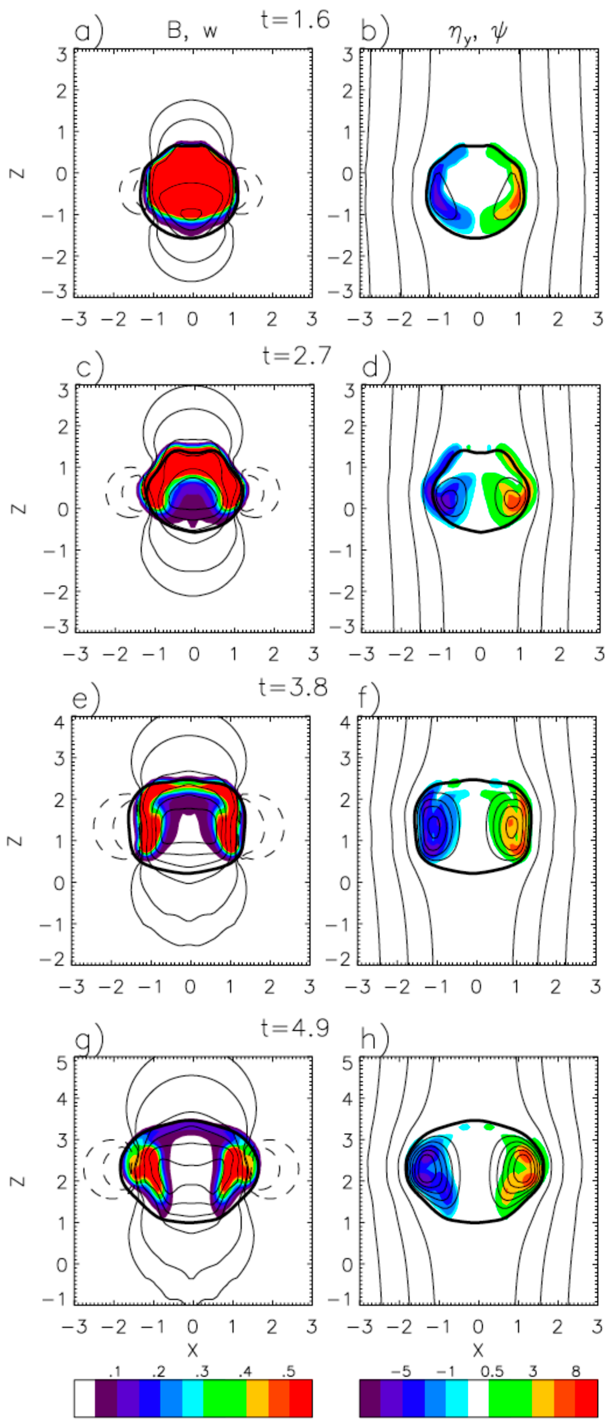

FIG. 5. As in Fig. 4, but for the $A_r = 1$ simulation during spinup at the times (t) indicated.

Profiles from the simulations are normalized by the maximum w with height normalized by the thermal depth; thermal bottom and top heights are set to −1 and 1, respectively. Correspondingly, $a = 1$ in (26) and (27) for the Hill's vortex w profile. All of the simulations produce similar w profiles as Hill's vortex, with the $A_r = 1$ being closest. There is also a close correspondence of the $A_r = 2$ simulation with Hill's vortex, with greater deviation for $A_r = 0.5$. Overall, these results support the discussion in section 2e on the validity of approximating σ for thermals from Hill's vortex.

Differences in spreading rate $\alpha \equiv dR/dz$ among the simulated thermals are seen in Fig. 7a, which shows thermal radius R as a function of z_t for the simulations with A_r of 0.5, 1, and 2. The increase of R with z_t is clearly greater as A_r is decreased, with α about 3 times larger in the $A_r = 0.5$ simulation compared to $A_r = 2$. Although R is somewhat noisy, the overall spreading rates are nearly constant with z_t (seen by the dotted lines) consistent with similarity theory.

A comparison of simulated w_t as a function of z_t with solutions to the analytic w_t equation, Eq. (11), is shown in Fig. 7b. The analytic w_t are obtained using mean values of C_v, b, and α from each simulation (Table 2). The overall behavior of w_t is similar among the simulations, with a sharp increase during spinup followed by a slower decrease after spinup. The analytic w_t are close to the simulated values for each simulation (compared the dotted and solid lines in Fig. 7). Larger values of α in the $A_r = 0.5$ simulation correspond to faster spinup and lower height of maximum w_t (critical height z_c) compared to the $A_r = 1$ and especially $A_r = 2$ simulations with smaller α. Thus, z_c increases with A_r consistent with the theory in section 2d.

Thermal behavior during spinup for the simulations with A_r of 0.5, 1, and 2 is further illustrated in Fig. 8, which shows time series of thermal top height z_t and vertical velocity w_t, circulation Γ, and vertically integrated core buoyancy ($\int B_c\,dz$). Also shown in Fig. 8 are the height z_p and vertical velocity w_p of a parcel placed initially at the thermal bottom that rises relative to the thermal as a whole. Consistent with the discussion in previous sections, Γ increases during spinup owing to $\int B_c\,dz > 0$ following (13), and this is accompanied by an increase in w_t. w_p increases relative to w_t as the parcel rises through the thermal core, with w_p reaching a maximum when the parcel is near the thermal's vertical midpoint. As a result of this velocity difference, z_p increases faster than z_t. Since the parcel is initiated on the thermal edge at its bottom, this marks the upward advance of entraining fluid into the thermal core (see also vertical cross sections of B in Fig. 5). This leads to a decrease in $\int B_c\,dz$ and the rate of increase in Γ slows (i.e., $d\Gamma/dt$ decreases). At the time when the parcel rises to near thermal top ($z_p \approx z_t$), $\int B_c\,dz$ reaches steady values near 0 (though somewhat larger in the $A_r = 2$ simulation) and $d\Gamma/dt \approx 0$. This point defines the time τ_c and height z_c of thermal spinup consistent with the discussion in section 2. The terms τ_c and z_c are calculated here as the time and height when z_p reaches within 2% of z_t. τ_c is denoted by the vertical black lines in Fig. 8. After spinup, z_p tracks closely to z_t and w_p remains close to w_t, while both decrease slowly. Overall, Γ (time-averaged past spinup) increases sharply as A_r is increased, from $\Gamma \approx 2.30$ for $A_r = 0.5$ to $\Gamma \approx 18.02$ for $A_r = 2$. Note that there is a small increase in Γ in the $A_r = 2$ simulation after spinup corresponding to a small but nonnegligible $\int B_c\,dz$ consistent with vertical cross sections of the B field (see Fig. 4c). This occurs because entrained fluid from below the thermal has $B > 0$ in this simulation; not all the initially

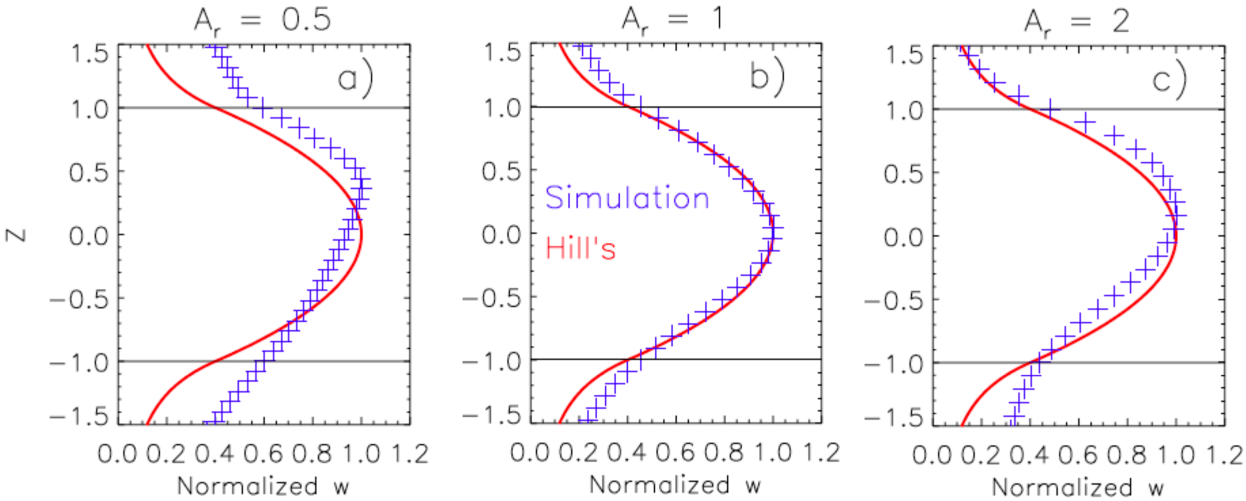

FIG. 6. Comparison of vertical profiles of w from the simulated thermals (blue crosses at each model level) with that from Hill's analytic spherical vortex (red lines). The thermal/vortex bottom and top heights are normalized to −1 and 1, respectively, and shown by the horizontal black lines. Profiles of nondimensional w are normalized such that the maximum value is 1. Simulation results are shown for (a) $A_r = 0.5$, (b) $A_r = 1$, and (c) $A_r = 2$ near the time of thermal spinup.

buoyant fluid is taken up by the thermal initially when the aspect ratio is large so that some remains below the thermal's circulation as discussed earlier. Values of $\int B_c\,dz$ reached in the $A_r = 2$ simulation after spinup appear to be nearly steady in time thereafter, and they are about an order of magnitude larger than in the other simulations after their spinup. It is expected that $\int B_c\,dz$ would eventually decrease in the $A_r = 2$ simulation as the thermal continued to rise and entrain, but investigating this would require longer simulations and thus a larger domain.

Values of z_c from the simulations, estimated from z_p and z_t as described above, are compared to the theoretical linear z_c–A_r relation (23) using $\sigma = 2$ from Hill's analytic vortex (see section 2e) and using the average $\sigma = 1.80$ from the simulations (Table 2) in Fig. 9a. The simulated and theoretical z_c values are similar, although the $A_r = 2$ simulation deviates more substantially from the theoretical relations. Reasons for this deviation are unclear but might be explained by the buoyant fluid entrained into the thermal from below in this simulation, leading to some buoyancy

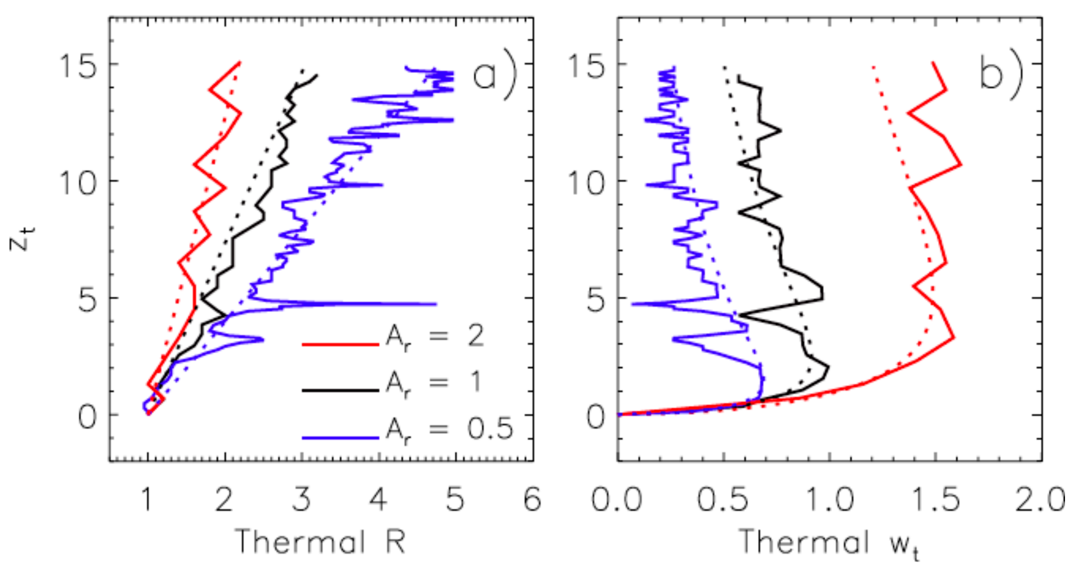

FIG. 7. Vertical profiles of (a) thermal radius R and (b) ascent rate w for simulations with various A_r as indicated. Solid lines show results calculated directly from the simulations. Dotted lines in (a) show fit values of constant $\alpha \equiv dR/dz$ and in (b) show solutions to the analytic w Eq. (11) using $C_d = 0$ and mean values of C_v, α, e from the simulations.

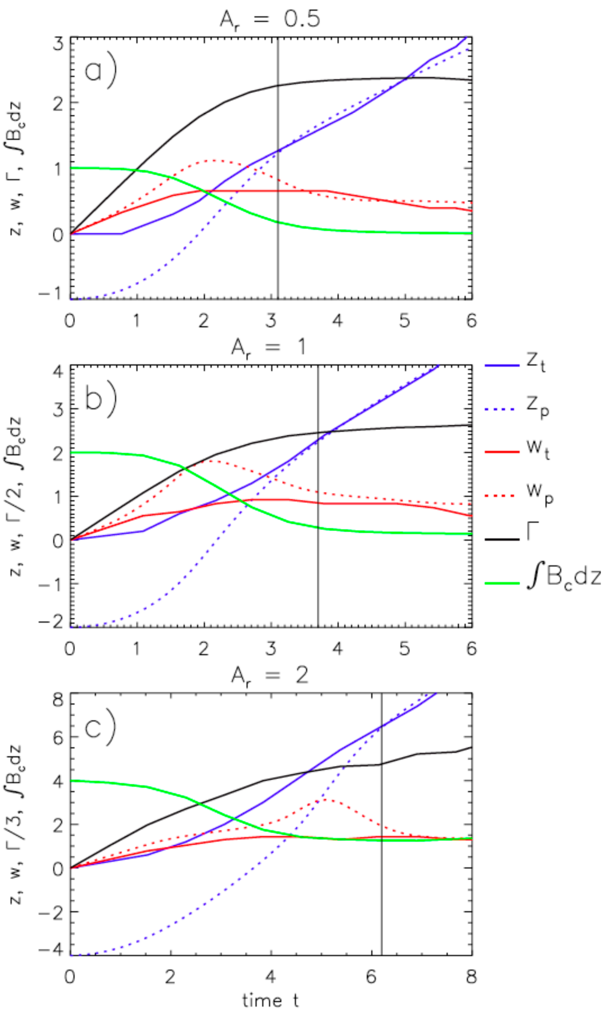

FIG. 8. Various nondimensional parcel and thermal properties as a function of time t during the thermals' spinup for simulations with (a) $A_r = 0.5$, (b) $A_r = 1$, and (c) $A_r = 2$. Results are shown for thermal top height z_t, parcel height z_p, thermal ascent rate w_t, parcel ascent rate w_p, thermal circulation Γ, and vertically integrated buoyancy along the thermal's central vertical axis B_c. The thermal top height at initial time ($t = 0$) is at $z = 0$. Parcels at $t = 0$ are centered horizontally at the thermal bottom and move upward through the thermal over time.

remaining along the thermal's vertical axis even after spinup. The theoretical $\sigma \approx 2$ derived from the Eulerian mean w of Hill's vortex (see section 2e) is fairly close to σ values obtained directly from the simulations (within 10% except for the $A_r = 2$ simulation), though somewhat larger. The simulated values range from 1.80 to 1.95 for $A_r < 2$ but are slightly smaller ($\approx$1.63) for $A_r = 2$ (see Table 2).

A direct comparison of the simulated and theoretical values of spreading rate α is shown in Fig. 9b. Theoretical values are obtained from 1) Eq. (19) using z_c and b derived from the simulations (Table 2), 2) Eq. (20) using z_c derived from the simulations and $b = 3$ following self-similarity, 3) Eq. (25) using the average $\sigma = 1.80$ from the simulations to predict z_c, and 4) Eq. (31) which calculates α from z_c predicted using $\sigma = 2$ from Hill's analytic vortex. All of the theoretical calculations for α give similar results as the simulations. The simulations show a sharp decrease of α with increasing A_r that follows an approximate A_r^{-1} dependence consistent with the theoretical expressions. Using $b = 3$ instead of b values obtained directly from the simulations leads to a small decrease in theoretical α. In this case, α values are somewhat smaller than simulated values for $A_r \geq 1$, but closer to simulated values for $A_r < 1$. Using (31) to calculate α well describes the α–A_r relation but with ~10% larger α compared to the simulations (solid line in Fig. 9b). This is consistent with the small overestimation of $\sigma = 2$ approximated from Hill's vortex. Using the average σ from the simulations ($\sigma = 1.80$) to predict z_c, and in turn α following (25), gives a close correspondence to the simulated α over the range of A_r (dotted line in Fig. 9b).

5. Discussion

Overall, the simulations and theory are in reasonable agreement regarding thermal top height at spinup z_c and thermal spreading rate α and how they vary with initial aspect ratio A_r. Our results indicate a nearly linear relation between z_c and A_r (though with greater deviation for the $A_r = 2$ simulation) and an inverse relation between α and A_r ($\alpha \propto A_r^{-1}$). Qualitatively, this α–A_r relation is consistent with previous thermal studies (see Fig. 17 in Lai et al. 2015). Larger α is associated with greater fractional entrainment rate which leads to a lower critical height z_c, defined as the thermal top height when w_t is maximum. z_c also corresponds to the thermal top height when buoyant fluid along the thermal's vertical axis is replaced by nonbuoyant environmental fluid entrained and advected upward through the thermal core, after which the thermal is spun up and $d\Gamma/dt \approx 0$. The time scale for this process is controlled by how long it takes for parcels initially just below the thermal bottom to ascend through the thermal, which in turn depends on A_r. By relating to α to z_c, and z_c in turn to A_r, we obtained the inverse relation between α and A_r in section 2.

This explains why larger α is associated with smaller A_r but does not by itself explain the physical mechanism. A key question, therefore, is what is the mechanism *driving* the increase in α as A_r is reduced? With small A_r, $\int B_c\, dz$ is relatively small, and thus, Γ increases slowly. This implies that at a given nondimensional time, Γ will be small relative to that for a thermal with larger A_r. As entrained fluid rises through the thermal and sweeps out buoyant fluid along the thermal's vertical axis, baroclinic generation and destruction of vorticity spread the vortex ring and hence thermal boundaries outward (McKim et al. 2020; also see Fig. 9 in Morrison et al. 2021). This buoyant forcing will have a relatively greater impact on the vorticity field when Γ is small, thus leading to faster outward spread and larger α when A_r is small. This is consistent with the impulse–circulation relation expressed by (16) after spinup when $d\Gamma/dt \approx 0$. That equation shows that for a given domain-integrated buoyant forcing F_B, smaller Γ necessitates a larger increase in vortex ring radius R_v. Note that we cannot simply relate α to A_r using the impulse–circulation equation

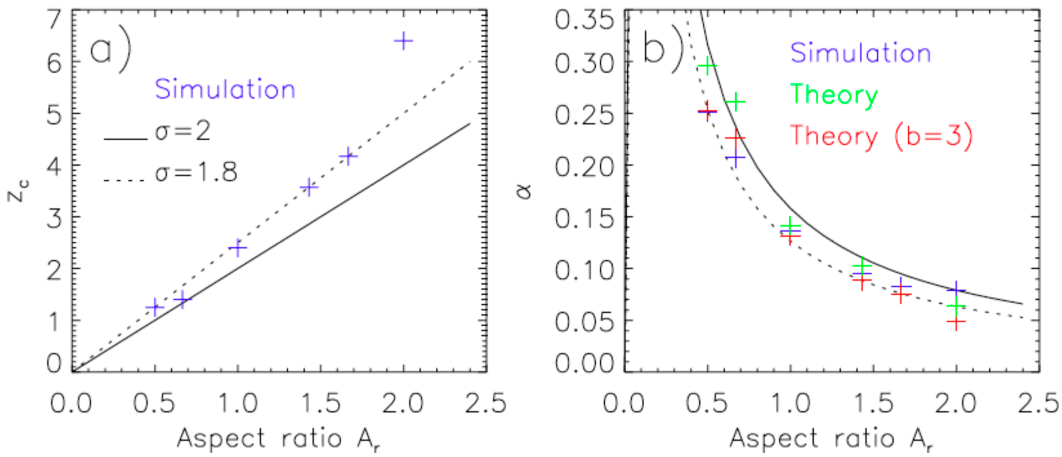

FIG. 9. (a) Critical height z_c and (b) thermal expansion rate α as functions of initial thermal aspect ratio A_r from the simulations and theory. α and z_c obtained directly from the simulations are shown by blue crosses. Green and red crosses in (b) show theoretical α values from (19) with b obtained from the simulations or 20 with $b = 3$, respectively, with z_c in both expressions obtained directly from the simulations. The theoretical z_c from (23) using $\sigma = 2$ from Hill's analytic vortex and using $\sigma = 1.8$ (average σ from the simulations) are shown by the solid and dotted black lines, respectively. The solid and dotted black lines in (b) show theoretical α values from (25) using $\sigma = 2$ and 1.8, respectively.

because Γ appears directly in this equation, and it depends on A_r in a nonstraightforward way. The change in impulse over time, $dI_z/dt = F_B$, also varies with A_r. Moreover, α is defined by the change in thermal radius with thermal top height rather than over time, and thus, relating α directly to dI_z/dt and circulation requires a transformation of variables using $d/dt = w^{-1}d/dz$. These complications motivated us to instead relate α to A_r via z_c, from which we derived the simple $\alpha \propto A_r^{-1}$ scaling as noted above. Nonetheless, relations between impulse, buoyant forcing, circulation, and thermal/vortex ring radius provide a more complete picture of the physical mechanism underpinning this simple α–A_r relation.

This work also provides a concise explanation for why initially spherical thermals ($A_r = 1$) have $\alpha \approx 0.15$ (for an unstratified, neutrally stable environment). This value of α is intrinsically linked to the time scale for sweeping out of the buoyancy along the thermal's vertical axis and hence thermal spinup, which itself depends on the ratio (σ) of time-averaged w_p to w_t. The thermals' internal flow structures are similar to Hill's analytic spherical vortex, implying $\sigma \approx 2$ and in turn constraining the proportionality constant in the $\alpha \propto A_r^{-1}$ relation to $\approx$0.15 (see section 2e).

An interesting feature is that, in a given simulation, α is similar before and after thermal spinup. This is evident directly from the simulations (profiles of R in Fig. 7a, although they are somewhat noisy, and the vertical cross sections of thermal properties during spinup in Fig. 5), as well as indirectly by closeness of the simulated and theoretical w profiles (Fig. 7b), the latter calculated assuming constant α. Thus, α values are "locked in" early in the simulations, and they depend strongly on the initial conditions. Why is α similar during spinup and after? A possible explanation is that circulation is small early in the simulations, while at the same time, entrainment has only just begun to erode buoyancy in the thermal core. This means that buoyancy gradients and hence baroclinic generation and destruction of vorticity near the central core are weak (vorticity generation being concentrated more along the thermal boundary). However, because circulation and vorticity near the vortex core are also weak, the net result is a similar thermal spreading rate compared to later when both baroclinic generation/destruction of vorticity and circulation are stronger. Moreover, α is the change in R with z_t, and small w during early spinup means that a small spreading rate in time is associated with a relatively larger α.

We also note that α is somewhat larger for turbulent compared to laminar thermals; LJ2019 and Morrison et al. (2022) found ~20% and 40% larger values for turbulent thermals, respectively. At high Reynolds number, turbulent stresses lead to a spindown of circulation after thermal spinup such that $d\Gamma/dt < 0$ (Nikulin 2014; McKim et al. 2020). All else equal, $d\Gamma/dt < 0$ implies a larger spreading rate following the impulse–circulation relation (16). Nikulin (2014) developed an analytic expression for α as a function of Γ, F_B, an empirical parameter β (encapsulating ζ, C_v, and m), and an empirical proportionality constant characterizing the impact of turbulent stresses. Using parameter values deduced from experimental data, they suggested a ~3% increase in α from turbulent stresses. However, this study did not consider the effects of turbulent stresses on thermals starting from rest. Reduced circulation from turbulent stresses during spinup might explain the order-of-magnitude larger impact on α found by LJ2019 and Morrison et al. (2022), as both studies simulated thermals that were initially motionless. The hypothesis that turbulent stresses during spinup cause most of the differences in α between laminar and turbulent thermals is consistent with Fig. 3 in McKim et al. (2020), which shows that the turbulent case has ~30% smaller Γ at the time of spinup relative to the laminar case.

6. Summary and conclusions

This study investigated the spreading rate α and entrainment behavior of dry, buoyant thermals with varying initial aspect ratio A_r. An expression was derived for the nondimensional thermal ascent rate w_t as a function of thermal top height z_t from the thermal w momentum budget. From this expression, we defined a critical thermal top height z_c where $dw_t/dz_t = 0$. The height z_c corresponds to the thermal top height when buoyancy is eroded along the thermal's vertical axis from entrainment of nonbuoyant environmental fluid (with thermal circulation approximately constant thereafter). We then analytically solved $dw_t/dz_t = 0$ to derive an expression relating α and z_c. In turn, z_c depends on A_r and the ratio σ of the mean vertical velocity of a parcel rising from thermal bottom to near its top along its vertical axis to w_t. By approximating the thermal flow similarly to Hill's analytic spherical vortex, it was estimated $\sigma \approx 2$. In this way, we derived an analytic expression for α that depends inversely on A_r.

Numerical simulations of thermals with A_r varying from 0.5 to 2 were analyzed and compared to the theoretical expressions. The analytic formulation for w_t well matched the thermal simulations over the range of A_r. Values of α calculated directly from the simulations were also close to the theoretical α over the range of A_r. Consistent with the theory, increasing A_r led to slower spinup owing to an increase in distance (relative to the thermal radius) for parcels to travel from thermal bottom to near top, meaning that core buoyancy was eroded more slowly by entrainment. Values of σ were similar among the simulations and ranged from 1.63 to 1.95, somewhat less than the theoretical $\sigma \approx 2$ based on the flow similarity between the thermals and Hill's vortex. This work also provided an explanation for why initially spherical thermals ($A_r = 1$) have $\alpha \approx 0.15$, which occurs because of the similarity of thermal flow to Hill's vortex. This gives $\sigma \approx 2$ and constrains the proportionality constant in the $\alpha \propto A_r^{-1}$ relation to $\approx$0.15. We emphasize that changes in z_c do not cause changes in α, but larger α is associated with lower z_c, and both are controlled by the erosion of buoyancy along the thermal's vertical axis driven by entrainment of nonbuoyant fluid. This process also dictates changes in circulation that are consistent with thermal spreading rates via the thermal impulse–circulation relation.

This study has elucidated factors controlling the spreading rate of dry buoyant thermals. This work is relevant to buoyantly driven atmospheric flows, especially those with a localized pulse source of buoyancy or steady source that leads to a chain of multiple thermals. In particular, numerous studies have noted the importance of buoyant thermals for cumulus convection in the atmosphere (e.g., Blyth et al. 2005; Damiani et al. 2006; Sherwood et al. 2013; Romps and Charn 2015; Hernandez-Deckers and Sherwood 2018; Morrison et al. 2020; Peters et al. 2020). Spreading rates of dry thermals may also indirectly impact cumulus entrainment rates by influencing the size of thermals at cloud base (Mulholland et al. 2021). Although Vybhav and Ravichandran (2022) suggested similar growth rates for dry and moist (cloud) thermals, Morrison et al. (2021) found that the spreading rate of moist thermals was almost a factor of 2 smaller than dry thermals for conditions typical of cumulus convection in the lower and middle troposphere. It is unclear how results from the current study might translate to cumulus thermals, given the impact of latent heating and cooling on their buoyancy distributions. Moreover, for buoyantly driven atmospheric flows at scales of interest, dry and moist thermals are generally turbulent. Nikulin (2014) suggested that the effects of turbulent stresses can be considered as an additional term leading to a small increase in α. This is supported by the recent numerical modeling studies of LJ2019 and Morrison et al. (2022), although they demonstrated an order-of-magnitude larger impact on α than Nikulin (2014) (~20%–40% versus a few percent). Future work should refine understanding of the entrainment behavior and spreading rates for dry and moist turbulent thermals.

Acknowledgments. HM was supported by the U.S. Department of Energy Atmospheric System Research Grant DE-SC0020104. The National Center for Atmospheric Research is sponsored by the National Science Foundation. We acknowledge high-performance computing support from Cheyenne (DOI:10.5065/D6RX99HX) provided by NCAR's Computational and Information Systems Laboratory. We thank Dr. Steven Sherwood for helpful discussions and Dr. George Bryan for developing and maintaining CM1.

Data availability statement. This study used CM1 version 20.1 (cm1r20.1) released on 25 August 2020. CM1 code and detailed documentation are available at https://www2.mmm.ucar.edu/people/bryan/cm1/. Configuration and namelist files for the CM1 simulations as well as analysis code can be made available upon request to the first author.

APPENDIX

List of Symbols

a	Radius of Hill's vortex
A	Thermal cross-sectional area
A_r	Initial thermal aspect ratio
b	Parameter defined by the ratio e to α
B	Buoyancy
B_c	Core buoyancy along the thermal's vertical axis
B_{eff}	Effective buoyancy
C_d	Dynamic drag coefficient
C_v	Virtual mass parameter
D	Distance traveled by the vortex as a whole over time period Δt
D_0	Initial thermal vertical length
e	Entrainment efficiency
E	Momentum entrainment
E_u	Euler number
f	Fractional distance from vortex center where the parcel is initiated relative to radius a
F_d	Thermal-averaged pressure drag force
F_r	Froude number
F_{pB}	Thermal-averaged buoyant pressure drag force
F_{pD}	Thermal-averaged dynamic pressure drag force
g	Gravitational acceleration

I	Fluid impulse
I_z	Fluid impulse in the z direction
$\hat{\mathbf{k}}$	Unit vector in the vertical
k_1	Integration constant
m	Shape parameter defined as the ratio of V to R^3
p	Pressure
$\hat{\mathbf{n}}$	Unit vector normal to the thermal's surface
$\mathbf{u}$	Fluid velocity vector
$u_{\rm axi}$	Regridded radial velocity in cylindrical coordinates
$\mathbf{u}_b$	Displacement rate of thermal boundary
$\mathbf{u}_e$	Effective entrainment velocity
r	Radial direction in axisymmetric coordinates
R	Thermal radius
R_e	Reynolds number
R_v	Ring vortex radius
S	Region defined by circuit passing through the thermal core and returning through the ambient fluid
t	Time
V	Thermal volume
w	Fluid vertical velocity
W	Velocity of Hill's vortex
$w_{\rm axi}$	Regridded vertical velocity in cylindrical coordinates
w_p	Vertical velocity of a parcel along its Lagrangian path
w_t	Vertical velocity of thermal top
z	Height
$z_{\rm bs}$	Height at the bottom of region S
z_c	Thermal top height at spinup
z_t	Height of thermal top
$z_{\rm ts}$	Height at the top of region S
α	Rate of increase in thermal radius with height as the thermal rises, equivalent to dR/dz
γ	Thermal shape parameter defined as the ratio AR/V
Γ	Thermal circulation
ΔL_m	Grid spacing of the numerical model
Δt	Time for parcel to travel from near vortex bottom to near its top
ϵ	Fractional entrainment rate
η_y	Horizontal vorticity in the y direction
ω_ϕ	Azimuthal vorticity
Ω	Region of space occupied by thermal
ψ	Streamfunction
θ	Potential temperature
ρ	Fluid density
ρ_0	Constant background fluid density
σ	Ratio of time-averaged vertical velocities of the parcel and thermal top
τ_c	Time scale for thermal top to reach z_c
ζ	Ratio of ring vortex radius to thermal radius

REFERENCES

Akhmetov, D. G., 2009: *Vortex Rings*. Springer, 151 pp., https://doi.org/10.1007/978-3-642-05016-9.

Batchelor, G. K., 2000: *An Introduction to Fluid Dynamics*. Cambridge University Press, 615 pp.

Blyth, A. M., S. G. Lasher-Trapp, and W. A. Cooper, 2005: A study of thermals in cumulus clouds. *Quart. J. Roy. Meteor. Soc.*, **131**, 1171–1190, https://doi.org/10.1256/qj.03.180.

Bond, D., and H. Johari, 2005: Effects of initial geometry on the development of thermals. *Exp. Fluids*, **39**, 591–601, https://doi.org/10.1007/s00348-005-0997-1.

——, and ——, 2010: Impact of buoyancy on vortex ring development in the near field. *Exp. Fluids*, **48**, 737–745, https://doi.org/10.1007/s00348-009-0761-z.

Damiani, R., G. Vali, and S. Haimov, 2006: The structure of thermals in cumulus from airborne dual-Doppler radar observations. *J. Atmos. Sci.*, **63**, 1432–1450, https://doi.org/10.1175/JAS3701.1.

Escudier, M. P., and T. Maxworthy, 1973: On the motion of turbulent thermals. *J. Fluid Mech.*, **61**, 541–552, https://doi.org/10.1017/S0022112073000856.

Gharib, M., E. Rambod, and K. Shariff, 1998: A universal time scale for vortex ring formation. *J. Fluid Mech.*, **360**, 121–140, https://doi.org/10.1017/S0022112097008410.

Hernandez-Deckers, D., and S. C. Sherwood, 2018: On the role of entrainment in the fate of cumulus thermals. *J. Atmos. Sci.*, **75**, 3911–3924, https://doi.org/10.1175/JAS-D-18-0077.1.

Hill, M. J. M., 1894: On a spherical vortex. *Philos. Trans. Roy. Soc.*, **A185**, 213–245.

Lai, A. C. H., B. Zhao, A. W.-K. Law, and E. E. Adams, 2015: A numerical and analytical study of the effect of aspect ratio on the behavior of a round thermal. *Environ. Fluid Mech.*, **15**, 85–108, https://doi.org/10.1007/s10652-014-9362-3

Launder, B. E., and D. B. Spaulding, 1974: The numerical computation of turbulent flows. *Comput. Methods Appl. Mech. Eng.*, **3**, 269–289, https://doi.org/10.1016/0045-7825(74)90029-2.

Lecoanet, D., and N. Jeevanjee, 2019: Entrainment in resolved, dry thermals. *J. Atmos. Sci.*, **76**, 3785–3801, https://doi.org/10.1175/JAS-D-18-0320.1.

McKim, B., N. Jeevanjee, and D. Lecoanet, 2020: Buoyancy-driven entrainment in dry thermals. *Quart. J. Roy. Meteor. Soc.*, **146**, 415–425, https://doi.org/10.1002/qj.3683.

Morrison, H., J. M. Peters, A. C. Varble, W. M. Hannah, and S. E. Giangrande, 2020: Thermal chains and entrainment in cumulus updrafts. Part I: Theoretical description. *J. Atmos. Sci.*, **77**, 3637–3660, https://doi.org/10.1175/JAS-D-19-0243.1.

——, ——, and S. C. Sherwood, 2021: Comparing growth rates of simulated moist and dry convective thermals. *J. Atmos. Sci.*, **78**, 797–816, https://doi.org/10.1175/JAS-D-20-0166.1.

——, N. Jeevanjee, and J.-I. Yano, 2022: Dynamic pressure drag on rising buoyant thermals in a neutrally stable environment. *J. Atmos. Sci.*, **79**, 3045–3063, https://doi.org/10.1175/JAS-D-21-0274.1.

Mulholland, J. P., J. M. Peters, and H. Morrison, 2021: How does LCL height influence deep convective updraft width? *Geophys. Res. Lett.*, **48**, e2021GL093316, https://doi.org/10.1029/2021GL093316.

Nikulin, V. V., 2014: Analytical model of motion of turbulent vortex rings in an incompressible fluid. *J. Appl. Mech. Tech. Phys.*, **55**, 558–564, https://doi.org/10.1134/S0021894414040026.

Norbury, J., 1973: A family of steady vortex rings. *J. Fluid Mech.*, **57**, 417–431, https://doi.org/10.1017/S0022112073001266.

O'Brien, V., 1961: Steady spheroidal vortices—More exact solutions to the Navier-Stokes equation. *Quart. Appl. Math.*, **19**, 163–168, https://doi.org/10.1090/qam/137415.

Peters, J. M., H. Morrison, A. C. Varble, W. M. Hannah, and S. E. Giangrande, 2020: Thermal chains and entrainment in cumulus updrafts. Part II: Analysis of idealized simulations. *J. Atmos. Sci.*, **77**, 3661–3681, https://doi.org/10.1175/JAS-D-19-0244.1.

Richards, J. M., 1961: Experiments on the penetration of an interface by buoyant thermals. *J. Fluid Mech.*, **11**, 369–384, https://doi.org/10.1017/S0022112061000585.

Romps, D. M., and A. B. Charn, 2015: Sticky thermals: Evidence for a dominant balance between buoyancy and drag in cloud updrafts. *J. Atmos. Sci.*, **72**, 2890–2901, https://doi.org/10.1175/JAS-D-15-0042.1.

Scorer, R. S., 1957: Experiments on convection of isolated masses of buoyant fluid. *J. Fluid Mech.*, **2**, 583–594, https://doi.org/10.1017/S0022112057000397.

Sherwood, S. C., D. Hernández-Deckers, M. Colin, and F. Robinson, 2013: Slippery thermals and the cumulus entrainment paradox. *J. Atmos. Sci.*, **70**, 2426–2442, https://doi.org/10.1175/JAS-D-12-0220.1.

Stevens, B., C. H. Moeng, and P. P. Sullivan, 1999: Large-eddy simulations of radiatively driven convection: Sensitivities to the representation of small scales. *J. Atmos. Sci.*, **56**, 3963–3984, https://doi.org/10.1175/1520-0469(1999)056<3963:LESORD>2.0.CO;2.

Tarshish, N., N. Jeevanjee, and D. Lecoanet, 2018: Buoyant motion of a turbulent thermal. *J. Atmos. Sci.*, **75**, 3233–3244, https://doi.org/10.1175/JAS-D-17-0371.1.

Turner, J. S., 1957: Buoyant vortex rings. *Proc. Roy. Soc. London*, **239A**, 61–75, https://doi.org/10.1098/rspa.1957.0022.

Vybhav, G. R., and S. Ravichandran, 2022: Entrainment in dry and moist thermals. *Phys. Rev. Fluids*, **7**, 050501, https://doi.org/10.1103/PhysRevFluids.7.050501.

Wang, C. P., 1971: Motion of an isolated buoyant thermal. *Phys. Fluids*, **14**, 1643–1647, https://doi.org/10.1063/1.1693659.

Wang, R. Q., A. W. K. Law, E. E. Adams, and O. B. Fringer, 2009: Buoyant formation number of a starting buoyant jet. *Phys. Fluids*, **21**, 125104, https://doi.org/10.1063/1.3275849.

Zhao, B., A. W. Law, A. C. Lai, and E. E. Adams, 2013: On the internal vorticity and density structures of miscible thermals. *J. Fluid Mech.*, **722**, R5, https://doi.org/10.1017/jfm.2013.158.